Cancer Cell
Article

CellPress

Depletion of Carcinoma-Associated Fibroblasts and Fibrosis Induces Immunosuppression and Accelerates Pancreas Cancer with Reduced Survival

Berna C. Özdemir,[1,2] Tsvetelina Pentcheva-Hoang,[3] Julienne L. Carstens,[1] Xiaofeng Zheng,[1] Chia-Chin Wu,[4] Tyler R. Simpson,[3] Hanane Laklai,[5] Hikaru Sugimoto,[1,2] Christoph Kahlert,[1,2] Sergey V. Novitskiy,[6] Ana De Jesus-Acosta,[7] Padmanee Sharma,[3] Pedram Heidari,[8] Umar Mahmood,[8] Lynda Chin,[4] Harold L. Moses,[6] Valerie M. Weaver,[5] Anirban Maitra,[9] James P. Allison,[3] Valerie S. LeBleu,[1,2] and Raghu Kalluri[1,2,*]

[1]Department of Cancer Biology, Metastasis Research Center, University of Texas MD Anderson Cancer Center, Houston, TX 77054, USA
[2]Division of Matrix Biology, Department of Medicine, Beth Israel Deaconess Medical Center and Harvard Medical School, Boston, MA 02115, USA
[3]Department of Immunology, University of Texas MD Anderson Cancer Center, Houston, TX 77054, USA
[4]Department of Genomic Medicine, University of Texas MD Anderson Cancer Center, Houston, TX 77054, USA
[5]Department of Surgery, University of California, San Francisco, San Francisco, CA 94143, USA
[6]Department of Cancer Biology, Vanderbilt University School of Medicine, Nashville, TN 37232, USA
[7]Department of Medical Oncology, Johns Hopkins Hospital, Baltimore, MD 21287, USA
[8]Department of Radiology, Massachusetts General Hospital, Boston, MA 02114, USA
[9]Departments of Pathology and Translational Molecular Pathology, Ahmad Center for Pancreatic Cancer Research, University of Texas MD Anderson Cancer Center, Houston, TX 77030, USA
*Correspondence: rkalluri@mdanderson.org
http://dx.doi.org/10.1016/j.ccr.2014.04.005

SUMMARY

Pancreatic ductal adenocarcinoma (PDAC) is associated with marked fibrosis and stromal myofibroblasts, but their functional contribution remains unknown. Transgenic mice with the ability to delete αSMA$^+$ myofibroblasts in pancreatic cancer were generated. Depletion starting at either noninvasive precursor (pancreatic intraepithelial neoplasia) or the PDAC stage led to invasive, undifferentiated tumors with enhanced hypoxia, epithelial-to-mesenchymal transition, and cancer stem cells, with diminished animal survival. In PDAC patients, fewer myofibroblasts in their tumors also correlated with reduced survival. Suppressed immune surveillance with increased CD4$^+$Foxp3$^+$ Tregs was observed in myofibroblast-depleted mouse tumors. Although myofibroblast-depleted tumors did not respond to gemcitabine, anti-CTLA4 immunotherapy reversed disease acceleration and prolonged animal survival. This study underscores the need for caution in targeting carcinoma-associated fibroblasts in PDAC.

INTRODUCTION

Pancreatic ductal adenocarcinoma (PDAC) is a near uniformly lethal disease with a dismal median survival of 4 to 6 months (Hidalgo, 2010; Korc, 2007). Despite years of efforts to design therapeutic approaches for pancreatic cancer, the use of conventional chemotherapy combination regimens with modest benefit remains the only option for the overwhelming majority of patients who present with advanced neoplasms. Revisiting the complex biology of PDAC in an unbiased manner is thus urgently required if we are to develop more effective therapies. The progress in generating genetically engineered mouse models faithfully mimicking human PDAC provides a unique opportunity to interrogate the functional contribution of the desmoplastic stromal reaction in PDAC, a defining feature of this carcinoma, which accounts for the majority of the tumor tissue volume

Significance

Pancreas cancer is associated with large amounts of stroma composed of collagen I and myofibroblasts, but their functional contribution remains unknown. Specific depletion of myofibroblasts using compound genetic mouse models of PDAC leads to aggressive tumors with diminished animal survival. Fewer myofibroblasts in human PDAC also correlate with reduced patient survival. Detailed studies show that myofibroblast loss decreases the ability of the immune system to control cancer associated with the persistence of regulatory T cells. Myofibroblast depletion did not improve gemcitabine's efficacy, but immunotherapy to revive immune attack prolonged mice's survival. This study demonstrates a protective role of myofibroblasts and suggests that targeting carcinoma-associated fibroblasts in pancreas cancer should be approached with caution.

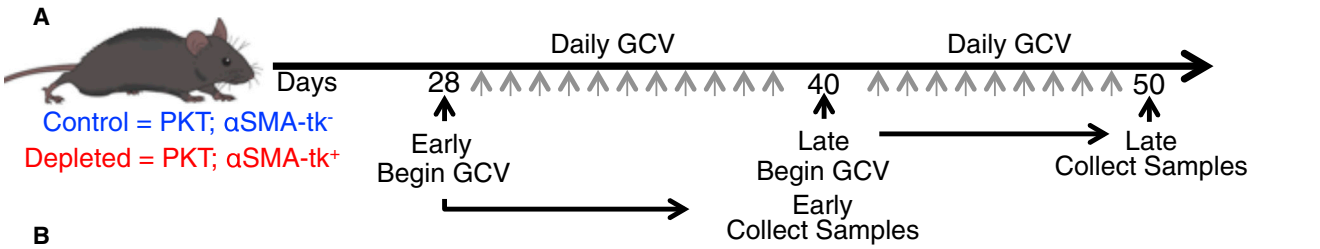

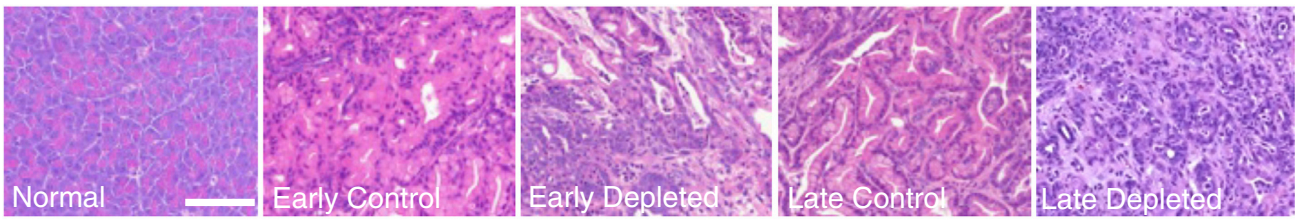

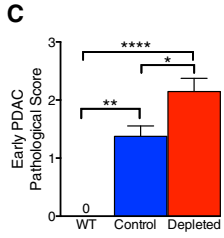

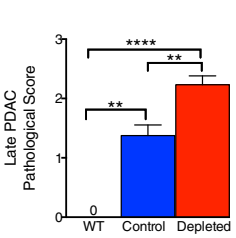

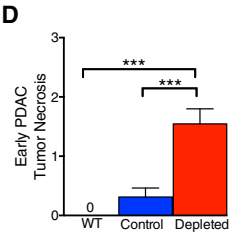

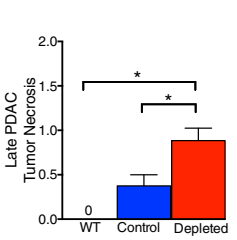

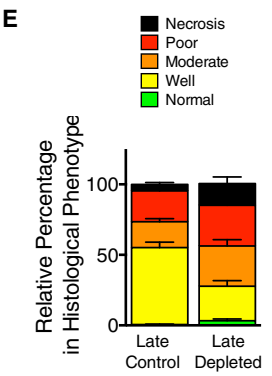

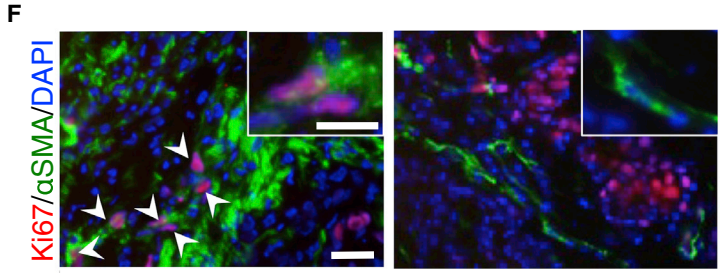

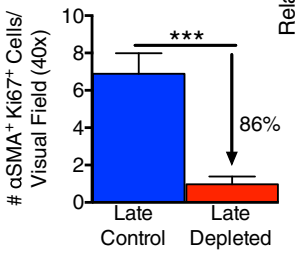

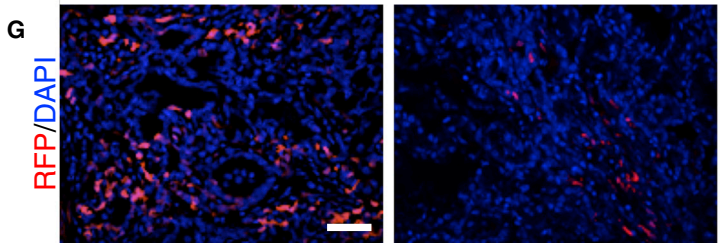

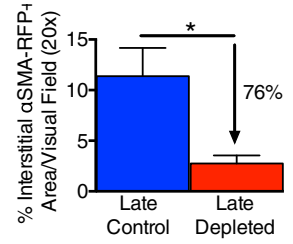

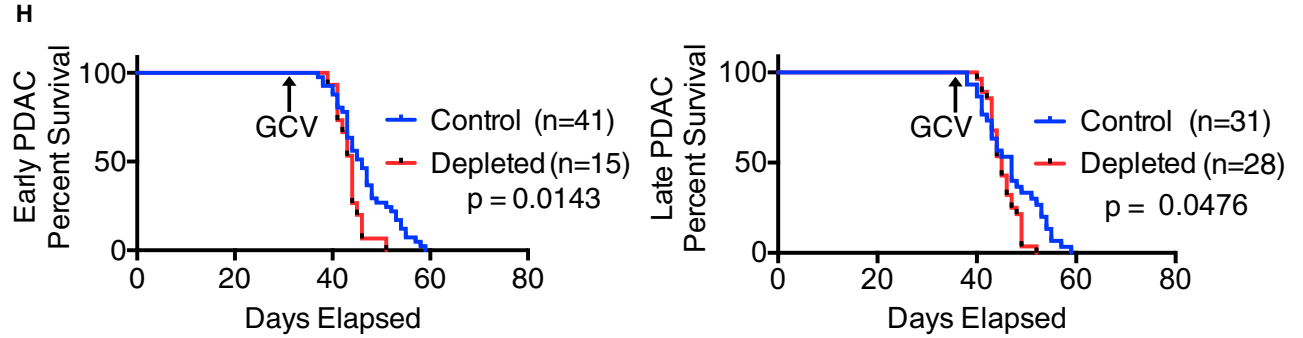

(legend on next page)

(Aguirre et al., 2003; Bardeesy et al., 2006a, 2006b; Gidekel Friedlander et al., 2009; Hingorani et al., 2003, 2005; Hruban et al., 2007; Ijichi et al., 2006).

The cellular component of the desmoplastic stroma in PDAC is composed primarily of myofibroblasts, characterized by αSMA expression (Feig et al., 2012; Rasheed et al., 2012). Recent studies have implicated the stroma as a physical barrier to the delivery of cytotoxic chemotherapies to the peritumoral milieu (Feig et al., 2012; Provenzano et al., 2012; Whatcott et al., 2012). Nonetheless, although preclinical models have demonstrated the benefit of stromal depletion through blockade of paracrine Hedgehog signaling in accentuating drug delivery (Olive et al., 2009), subsequent clinical trials targeting stromal myofibroblasts in human PDAC resulted in an apparent paradoxical accelerated disease progression, halting clinical trials (Amakye et al., 2013). These studies reinforced the need to critically evaluate the functional contribution of stroma in the initiation and progression of PDAC. In this regard, the functional role of αSMA^{+} myofibroblasts and type I collagen in PDAC remains unknown.

RESULTS

Myofibroblast Depletion Leads to Increased Tumor Invasion Associated with Decreased Survival

To interrogate the functional contribution of αSMA^{+} myofibroblasts in PDAC, we used a genetic strategy for selective in vivo depletion. *Ptf1a*$^{cre/+}$;*LSL-Kras*$^{G12D/+}$;*Tgfbr2*$^{flox/flox}$ (PKT) mice develop spontaneous PDAC with full penetrance that reliably recapitulates the clinical and histopathological features of the human disease (Ijichi et al., 2006). The mice consistently progress from pancreatic intraepithelial neoplasia (PanIN) at 4.5 weeks of age to invasive cancer at 6 weeks of age and die at 8 weeks of age, without much variation (Ijichi et al., 2006). These mice were crossed with αSMA-tk transgenic mice to selectively target proliferating αSMA^{+} myofibroblasts upon systemic ganciclovir (GCV; InvivoGen) administration (PKT; αSMA-tk mice) (LeBleu et al., 2013). Daily GCV injections were initiated when mice developed PanIN lesions (early) and allowed to progress to PDAC (Figure 1A). Mice also received GCV injections starting at the established PDAC stage (late) until they developed significant signs of illness leading to their death or requiring euthanasia (Figure 1A). In both early and late myofibroblast depletion settings, PKT mice presented with significantly more invasive, undifferentiated, and necrotic tumors when myofibroblasts were depleted compared with control tumors (Figures 1B–1E). Immunohistochemical and immunofluorescence analyses revealed an average of 80% depletion of proliferating myofibroblasts (Figure 1F; Figures S1A and S1B available online). Direct visualization of interstitial myofibroblasts using the αSMA-RFP transgenic mice crossed with PKT; αSMA-tk mice also showed approximately 80% depletion of total myofibroblasts (Figure 1G). A significant reduction in αSMA transcript level was also noted in depleted tumors (Figure S1C). Extrapancreatic organs, such as the kidney, lung, small bowel, heart, and liver, did not show any depletion in αSMA^{+} cells (Figures S1D and S1E). Notably, myofibroblast depletion in PDAC was associated with significant reduction in survival, in both the early and late depletion groups (Figure 1H). Tumor weight was significantly reduced by myofibroblast depletion and was associated with a reduced body weight specifically in PDAC mice with late myofibroblast depletion (Figures S1F and S1G). Mice with myofibroblast-depleted tumors exhibit an increased frequency of pulmonary emboli, likely contributing to diminished overall survival (Figure S1H).

Loss of one allele of *Tgfbr2* (versus both in the PKT mice) in the context of *Kras*^{G12D} activation (PKT^{Het} mice) leads to a similar PDAC phenotype, but with a slower progression rate, with PanIN lesions noted at 4 to 6 weeks of age and PDAC at 8 to 10 weeks of age (Ijichi et al., 2006). GCV treatment was initiated at the onset of PDAC in PKT^{Het}; αSMA-tk mice and continued until they died or were moribund, requiring euthanasia. Depletion of myofibroblasts resulted in undifferentiated tumors (Figures 2A–2E) and significantly diminished the survival of PKT^{Het}; αSMA-tk mice (Figure 2F). Similar findings were also observed when myofibroblasts were depleted in *Pdx1*$^{cre/+}$;*LSL-Kras*$^{G12D/+}$;*Trp53*$^{R172H/+}$ (KPC) mice crossed with αSMA-tk (KPC; αSMA-tk) mice. Myofibroblast depletion in this setting also resulted in poorly differentiated tumors and significantly diminished survival (Figures S2A–S2C). Because of the similar phenotypes of the PKT; αSMA-tk mice and KPC; αSMA-tk mice, the remaining experiments were carried out using the PKT mice because of their faster course of disease.

On the basis of the striking and somewhat unexpected impact of stromal depletion on survival in PDAC models, we next assessed whether a comparable impact of stromal content was observed in the cognate human setting. Immunohistochemical scoring for interstitial αSMA^{+} cells from resected PDAC of untreated patients indicated that low αSMA is associated with

Figure 1. Myofibroblast Depletion Augments PDAC and Diminishes Overall Survival

(A) Tumor progression timeline with experimental treatment time points. GCV administration in PKT; $\alpha SMA\text{-}tk^{+}$ mice allows myofibroblast depletion, in contrast with control PKT; $\alpha SMA\text{-}tk^{-}$ mice.

(B) Representative micrographs of H&E stained pancreatic samples (scale bar represents 100 μm).

(C) Pathological scores of early-depleted tumors (left: wild-type [WT], n = 5; control, n = 16; depleted, n = 17) and late-depleted tumors (right: WT, n = 5; control, n = 17; depleted, n = 26). Significance was determined by one-way ANOVA with Tukey post hoc analysis.

(D) Necrosis penetrance of early-depleted tumors (left: WT, n = 5; control, n = 16; depleted, n = 22) and late-depleted tumors (right: WT, n = 5; control, n = 17; depleted, n = 25).

(E) Relative percentages in histological phenotypes in late depleted tumors. Control, n = 17; depleted, n = 25.

(F) Representative micrographs (scale bar represents 50 μm) of Ki-67/αSMA dual-immunofluorescence (left, control; right, depleted) and corresponding quantification (n = 4 and n = 6 for control and depleted, respectively). Arrows point to double-positive cells and inserts show high-magnification images (scale bar represents 25 μm).

(G) Representative micrographs (scale bar represents 100 μm) of reporter αSMA-RFP tumor samples (left, control; right, depleted) and corresponding quantification (n = 3 in each group).

(H) Survival analysis of early (left) and late (right) treatment groups. GCV, GCV treatment was initiated.

Data are represented as mean ± SEM. Unless otherwise noted, significance was determined using t tests (*$p < 0.05$, **$p < 0.01$, ***$p < 0.001$, ****$p < 0.0001$). ns, not significant. See also Figure S1.

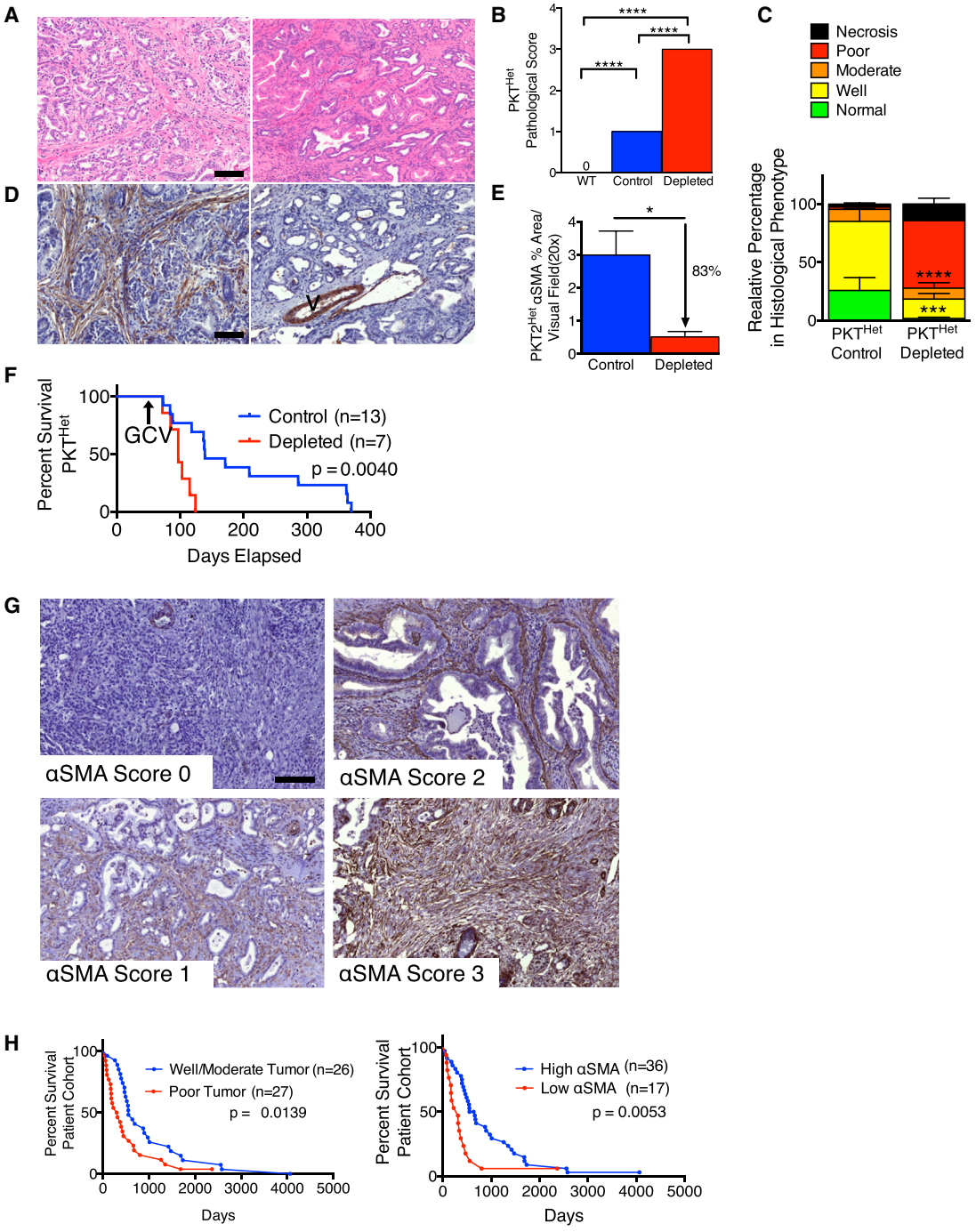

Figure 2. Decreased αSMA Correlates with Poor Prognosis and Overall Survival in Slow-Progressing Mice with PDAC and Patients with Pancreatic Cancer

(A and B) Representative micrographs of H&E stained PKT^{Het} tumors at 106 (control, left) and 103 (depleted, right) days old (A) (scale bar represents 100 μm) and pathological scores (B). WT, n = 5; control, n = 6; depleted, n = 4. Significance was determined by one-way ANOVA with Tukey post hoc analysis.

(C) Relative percentages in histological phenotypes (n = 6 and n = 4, respectively, for control and depleted).

(D and E) Representative micrographs of αSMA stained pancreatic samples as in (A) (D) (scale bar represents 100 μm) and corresponding quantification (E) (n = 6 and n = 4, respectively, for control and depleted). V, vessel.

(F) Survival analysis in PKT^{Het} mice. GCV, GCV treatment was initiated.

(G) Representative micrographs of αSMA stained pancreatic samples resected from patients in each score category: 0, 1, 2, and 3 (scale bar represents 200 μm).

(H) Survival analysis based on histopathological score (left) and αSMA score (right). Low αSMA: scores 0 and 1; high αSMA: scores 2 and 3.

Significance was determined using the Mantel-Cox test. Data are represented as mean ± SEM. Unless otherwise noted, significance was determined using t tests (*p < 0.05, ***p < 0.001, ****p < 0.0001). ns, not significant. See also Figure S2 and Table S1.

worse survival, supporting the observations in the PKT and KPC mice with myofibroblast depletion (Figure 2G; Table S1). Of note, patients with low αSMA scores present significantly more often with poorly differentiated cancers than tumors with well or moderate differentiation (Table S1), and yet despite this correlation, αSMA scoring offered greater significance in differential stratification of patients for survival than histopathological grade (Figure 2H), suggesting that stromal content likely has a direct impact on the natural history of human PDAC.

Myofibroblast Depletion Reduced Type I Collagen Content and Altered Extracellular Matrix Organization in PDAC

Global gene expression profiling of tumors from PKT mice without (control) and with myofibroblast depletion (depleted) revealed differentially expressed genes associated with remodeling of the extracellular matrix (ECM), epithelial-to-mesenchymal transition (EMT), angiogenesis, and immune response (Table S2). Comparative analyses of tumor transcriptomes revealed 4,393 differentially expressed genes in early-depleted versus age-matched control tumors (1,682 downregulated and 2,711 upregulated genes) and 2,344 differentially expressed genes in late-depleted versus age-matched control tumors (1,170 downregulated and 1,174 upregulated genes) (Figures S3A–S3D). Tumor collagen content assayed by type I collagen immunostaining (Figure 3A) was significantly decreased in myofibroblast-depleted tumors. Masson's trichrome staining (MTS) and picrosirius red staining revealed a significant reorganization of collagen fibrils, with decreased stiffness and elastic modulus in myofibroblast-depleted tumors compared with control tumors (Figures 3B–3D). Interestingly, collagen crosslinking and immunolabeling for the collagen crosslinking enzyme lysyl oxidase (LOX) were unchanged despite reduced stiffness of the ECM (Figures 3E and 3F), highlighting a complex regulation of type I collagen crosslinking mediated by multiple sources of LOX. These results are consistent with the ability of αSMA^+ myofibroblasts to produce type I collagen and induce fibrosis in PDAC. Despite extensive remodeling of type I collagen ECM in myofibroblast-depleted tumors, hyaluronic acid (HA) binding protein (HABP), a marker for total HA content, remained unchanged in the myofibroblast-depleted tumors (Figure S3E). Vimentin labeling, however, was significantly decreased in myofibroblast-depleted tumors (Figure S3F). Auditing of other mesenchymal cells in the PDAC tumor stroma revealed a decrease in the number of fibroblast-specific protein 1 (FSP1)/$S100A4^+$ cells in myofibroblast-depleted tumors (Figure S3G), while the number of fibroblast activation protein (FAP)-positive cells remained unchanged (Figure S3H). Colocalization of αSMA with FAP was not detectable in the PDAC tumors (Figure S3H).

Myofibroblast-Depleted PDAC Displays Suppression of Angiogenesis, Enhanced Tumor Hypoxia, EMT Program, and Cancer Stem Cell-like Phenotype

Histopathological analyses of myofibroblast-depleted tumors revealed highly undifferentiated, invasive-grade tumors with enhanced necrosis (Figures 1B–1E). These features are associated with tumor hypoxia and the acquisition of an EMT program. Myofibroblast depletion was associated with a decrease in the number of $CD31^+$ vessels, indicative of suppressed vessel density (Figure 4A; Figures S4A–S4C). Perivascular αSMA^+ cells appear unaffected by the αSMA-tk strategy (Figure S4A). Global gene expression profiling performed on normal pancreas fibroblasts and PDAC-associated fibroblasts (CAF) shows differences in pathways affecting ECM remodeling, angiogenesis, and immune response in PDAC (Figure S4D; Table S3). RNA sequencing analyses further validated the increased expression of several proangiogenic factors in CAF, supporting their proangiogenic role in PDAC (Table S3).

Although pericyte numbers, assayed by immunostaining analyses for the pericyte marker NG2 (Figure S4B), and vascular leakage, determined by extravascular fluorescein isothiocyanate (FITC)-dextran (Figure 4B; Figure S4E), were unchanged, tumor hypoxia assayed by staining for pimonidazole adduct formation was dramatically increased in myofibroblast-depleted tumors compared with control tumors (Figure 4C; Figure S4F). Lineage tracing of cancer cells using the LSL-YFP reporter together with immunolabeling for αSMA allowed the quantitative analysis of YFP^+ cancer cells that have acquired mesenchymal features ($YFP^+\alpha SMA^+$ cells). Tumors with 80% depletion of αSMA^+ interstitial myofibroblasts showed an increase in EMT program with increased $YFP^+\alpha SMA^+$ cells (Figure 4D; Figure S4G) and enhanced expression of the EMT transcriptional regulators, *Twist*, *Snail*, and *Slug* (Figure 4E). The enhanced acquisition of EMT was associated with the loss of mucin staining (Figure S4H), which is in alignment with the decreased histological differentiation within the neoplastic glands (Figures 1B–1E). YFP^+ cancer cells from myofibroblast-depleted tumors exhibited an increase in their capacity to form spheres in culture, a feature of cells with EMT program and potential cancer stem cell-like phenotype (Kalluri and Weinberg, 2009; Scheel and Weinberg, 2012) (Figure 4F; Figure S4I). Additionally, the number of $CD44^+CD133^+$ cells (suggestive of pancreatic cancer stem cells; Hermann et al., 2007; Simeone, 2008) was enhanced in myofibroblast-depleted tumors (Figure 4G). Fluorescence-activated cell sorted YFP^+ cells freshly isolated from myofibroblast-depleted tumors showed enhanced tumorigenic potential when implanted in nude mice (Figure 4H). Interestingly, cancer cells with EMT program and expression of αSMA were not eliminated in the PKT; αSMA-tk mice on GCV administration but increased in number (Figure 4D). This could be explained by the observation that cancer cells with EMT program likely do not proliferate (Tsai et al., 2012; Vega et al., 2004), further confirming their low-cycling-stem-cell status. Further, although overall apoptosis was significantly increased in myofibroblast-depleted tumors (Figures S4J and S4K), it was mostly localized within terminally differentiated compartments, such as islets (Figure S4K).

Reduction of Fibrosis Does Not Increase the Efficacy of Gemcitabine in PDAC

To test whether the decrease in myofibroblasts and type I collagen content along with reduced ECM stiffness leads to increased efficacy of gemcitabine (GEM), we treated control and myofibroblast-depleted mice with GEM. Histopathological score did not improve when PKT mice were treated with GEM alone or in combination with myofibroblast depletion (Figure 5A). $TUNEL^+$ cell number increased with myofibroblast depletion, independent of GEM treatment, and GEM treatment alone did not significantly increase tumor cell apoptosis (Figure 5B). Similarly,

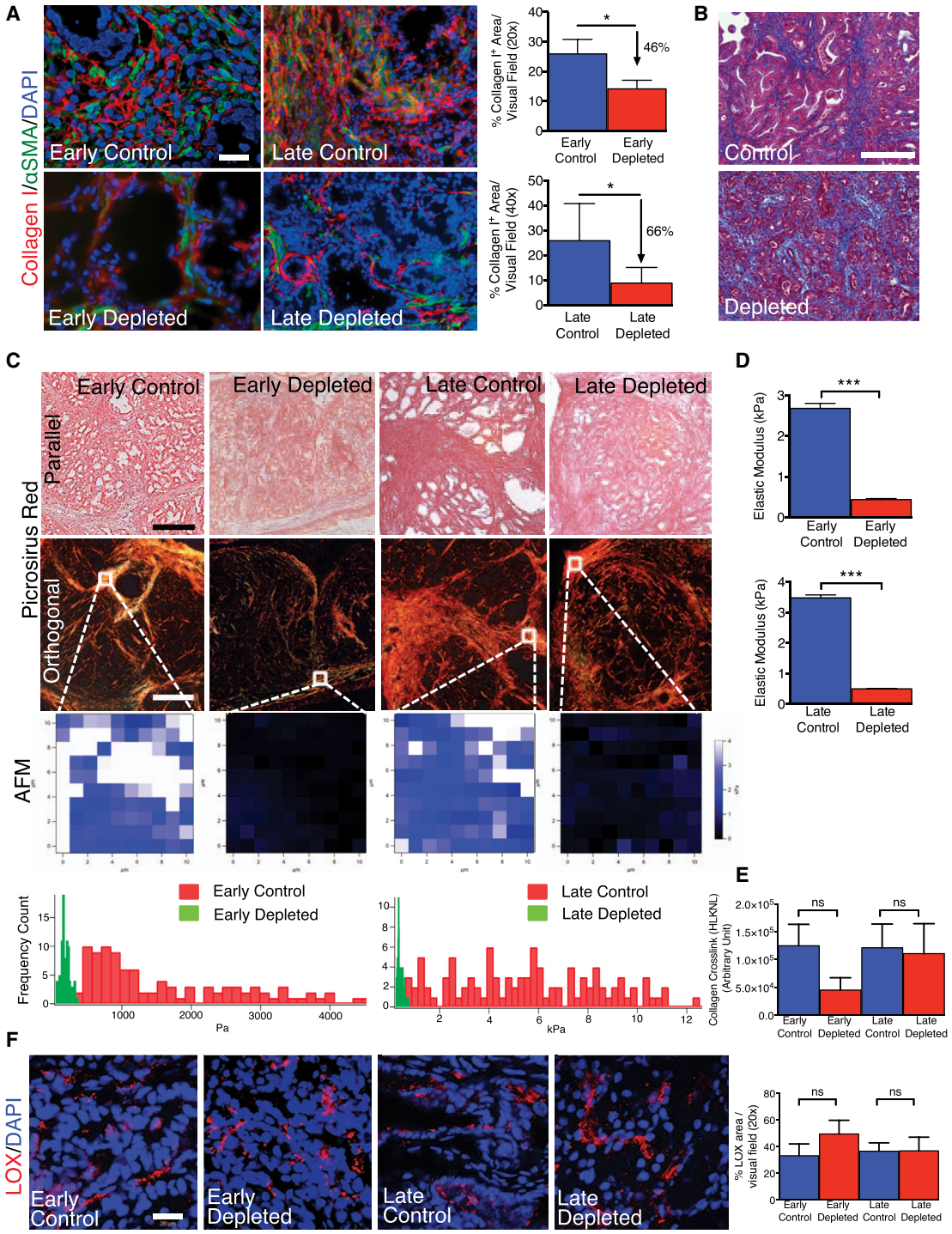

Figure 3. PDAC ECM Is Significantly Remodeled in Myofibroblast-Depleted Tumors

(A) Representative micrographs (scale bar represents 50 μm) of collagen I and αSMA and corresponding quantification (n = 4).

(B) Representative micrographs (scale bar represents 200 μm) of MTS in late control and late deleted mice.

(C) Representative images of picrosirius red staining of PKT pancreatic tissues samples viewed under parallel (top row) and polarized (second row) light (scale bar represents 75 μm) and representative images of stiffness distribution by atomic force microscopy measurement (AFM; third row) and quantification (bottom row, n = 3).

(D) Quantification of the elastic modulus of tumor matrix (n = 3).

(E) Collagen crosslinking quantification (n = 4).

(F) Representative micrographs for LOX (scale bar represents 20 μm) and quantification.

Data are represented as mean ± SEM. Significance was determined using t tests (*p < 0.05, ***p < 0.001). ns, not significant. See also Figure S3 and Table S2.

the change in FSP1$^+$ cells correlated only with myofibroblast depletion and was independent of GEM treatment (Figure 5C). Interestingly, CD31$^+$ cell numbers decreased with GEM therapy and decreased further with myofibroblast depletion (Figure 5D). Standard uptake values computed from ^{18}F-fluorodeoxyglucose positron emission tomography (PET)/computed tomography (CT) revealed comparable glycolysis per tumor volume in control, depleted, and GEM therapy in depleted tumors (Figure 5E). Despite a robust decrease in collagen content associated with myofibroblast depletion (fibrosis) (Figure 5F), GEM therapy did not improve overall survival (Figure 5G). Further, GEM therapy of PDAC compared with untreated mice did not result in improved survival, as previously reported using a different PDAC mouse model (Olive et al., 2009) (Figure 5G). GEM therapy in myofibroblast-depleted tumors compared with myofibroblast-depleted tumors also failed to improve overall survival (Figure 5G).

Myofibroblast Depletion Decreases Overall Immune Infiltration in PDAC but Results in Increased Frequency of FoxP3$^+$ Treg Cells

Gene expression profiling and RNA sequence analyses comparing control tumors with myofibroblast-depleted tumors revealed a significant change in the expression of genes associated with tumor immunity, including those associated with acute inflammatory responses, regulation of macrophage activation, regulation of T cell-mediated cytotoxicity, antigen presentation, and B cell activation (Figure 6A; Table S2). Tumors with myofibroblast depletion starting at the PanIN stage (early) present with significant decreases in overall peritumoral infiltration of CD45$^+$ cells and CD3$^+$ T cell and CD19$^+$ B cell infiltration compared with control tumors (Figure S5A). Such reductions in T cells and B cells were not observed in established PDAC with myofibroblast depletion (late-stage depletion) (Figure S5A). Natural killer (NK) cell infiltration with myofibroblast depletion was unchanged following myofibroblast depletion (Figure S5A). In both early and late depletion settings, myofibroblast depletion was associated with a significant suppression in the percentage of effector T cells (Teff, CD4$^+$Foxp3$^-$) together with an increase in the percentage of regulator T cells (Treg, CD4$^+$Foxp3$^+$), leading to an overall decrease in the Teff/Treg ratio (Figures 6B–6D). Myofibroblast depletion resulted in increased Foxp3 and *Ctla4* expression assayed by immunohistochemistry (IHC) (Figure S5B) and real-time PCR analysis (Figure 6E), respectively, consistent with the enhanced Treg infiltration. The cytotoxic CD8$^+$/Treg ratio was also decreased in the myofibroblast-depleted tumor (Figure 6F), as well as CD3$^+$/CD11b$^+$ ratio (early depletion; Figure 6G). The percentages of Teff and Treg, respectively, correlate with disease progression and acceleration of PDAC associated with myofibroblast depletion (Figures 6H and 6I). The percentages of CD11b$^+$Ly6G$^+$ cells and granulocytes (CD11b$^+$Gr1$^+$F4/80$^-$) were also increased in late myofibroblast-depleted tumors (Figures 6J and 6K), whereas the percentage of macrophages (CD11b$^+$Gr1$^-$ F4/80$^+$) was suppressed (Figure 6L). The differential tumor immune infiltration in early versus late depletion is also substantiated by distinct expression patterns in respective tumor immune gene expression signature, with a selectively downregulated tumor immunity gene signature in late-depleted tumor (Figure 6A).

Anti-CTLA-4 Antibody Therapy Rescues Enhanced PDAC Progression upon Myofibroblast Depletion and Increases Overall Survival

Myofibroblast depletion starting at early- and late-stage tumors resulted in a decreased Teff/Treg ratio associated with increased CTLA-4 expression (Figures 6D and 6E). Therefore, we tested whether the Teff/Treg ratio in PDAC mice with myofibroblast depletion can be rescued by CTLA-4 checkpoint blockade. Anti-CLTA-4 antibody administration significantly improved histopathological scores associated with a reduction in undifferentiated cancer cells (Figure 7A). Despite similar myofibroblast depletion (Figure 7B), suggesting that anti-CTLA-4 per se did not alter myofibroblast number, anti-CTLA-4 antibody treatment induced tumor clearance and replacement by normal parenchyma in up to 25% of the organ (Figure 7C). Treatment with anti-CTLA-4 antibodies in the setting of stromal depletion not only resulted in a rescue of the phenotype of myofibroblast-depleted tumors but also attenuated PDAC progression, which was associated with a significant extension in overall survival (an average increase of 60% in lifespan) (Figure 7D). Such elongation of lifespan was associated with reduced frequency of pulmonary emboli (Figure 7E). This was noticed in concordance with restored Teff and Treg percentages (Figure 7F) and diminished tumor sphere-forming ability within remnant cancer cells in age-matched mice (Figure 7G). Further, the transcriptome of myofibroblast-depleted tumors treated with anti-CTLA-4 clustered with the expression profiles of control tumor rather than myofibroblast-depleted tumors, suggesting that transcriptional reprogramming accompanies the observed phenotypic rescue (clustering using the 2,344 differentially expressed genes in late-depleted tumors versus control) (Figure 7H). Anti-CTLA-4 alone did not alter αSMA$^+$ content, and histopathological analyses revealed a modest increase in the percentage of normal parenchyma (Figures S6A and S6B). Treatment with anti-CTLA-4 alone improved overall survival (median survival of 49.5 days, compared with 47 days in the control group), albeit to a much lesser extent than anti-CTLA-4 treatment in combination with fibrosis depletion (median survival of 65 days) (Figure 7D).

DISCUSSION

The desmoplastic reaction is thought to represent a host defense mechanism, similar to wound healing and tissue regeneration, to repair or hopefully impede the conversion of a neoplastic lesion into invasive carcinoma (Bissell and Radisky, 2001; Dvorak, 1986; Lu et al., 2012). The function of desmoplastic stroma is likely dynamic during cancer progression, and its heterogeneous cellular and noncellular constituents change in relation to the evolving genetic landscape of cancer cells. In this regard, several studies have suggested that αSMA$^+$ myofibroblasts and type I collagen associated with tumor fibrosis are tumor promoting in solid tumors, including PDAC (Angeli et al., 2009; Karnoub et al., 2007; Merika et al., 2012; Vong and Kalluri, 2011). We demonstrate that depletion of αSMA$^+$ myofibroblasts resulted in multiple adverse outcomes leading to poor survival. These results suggest that at both early and late stages of pancreatic cancer, fibrosis associated with myofibroblasts and type I collagen constitutes a protective response from the host rather

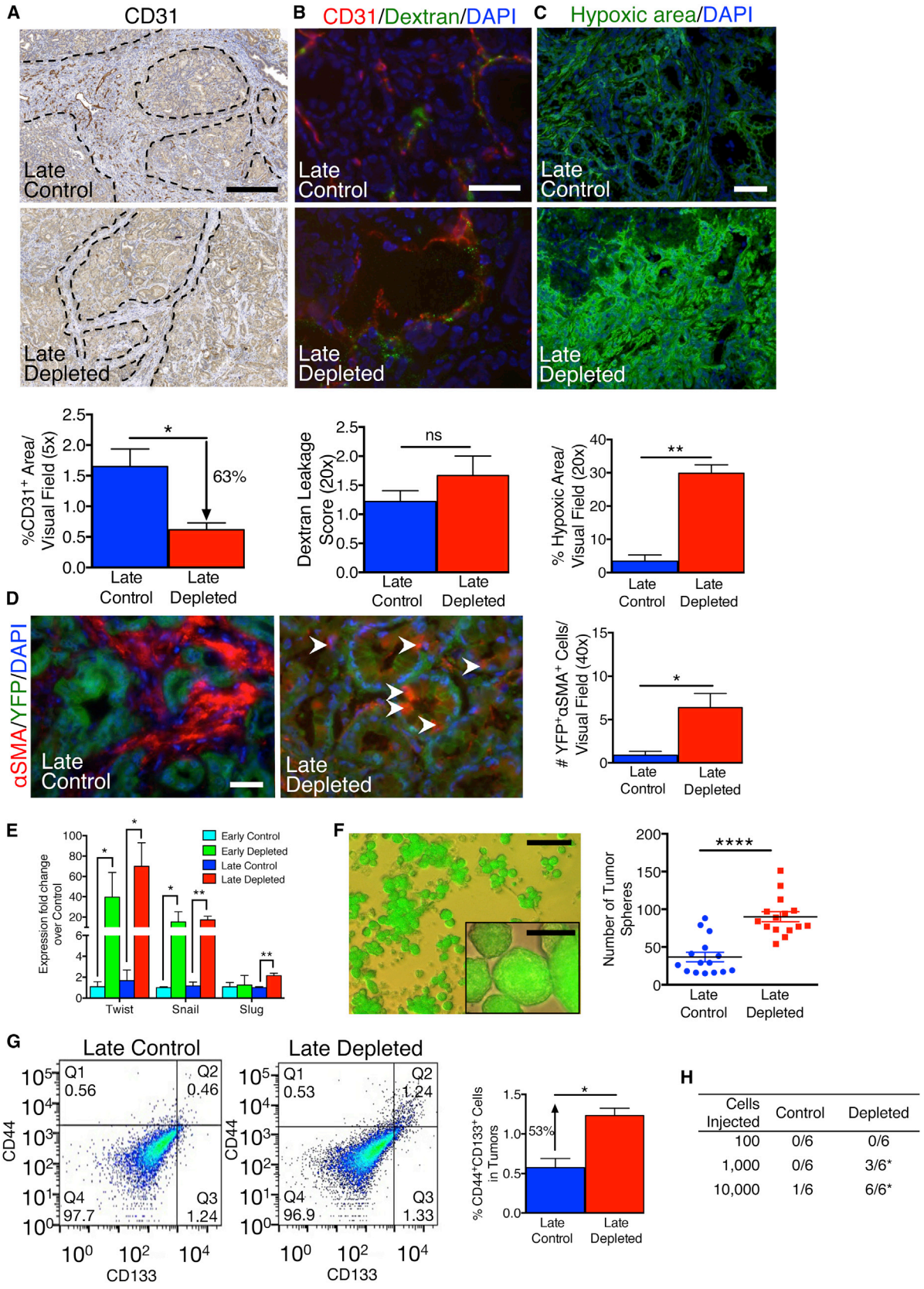

(legend on next page)

than offering an oncogenic supportive role, as speculated (Armstrong et al., 2004; Omary et al., 2007). This conclusion is supported by the clinical correlation between high αSMA and improved survival; a similar trend was previously reported from analyses also performed on resected tumors from treatment-naive patients (Wang et al., 2013). Although other studies have also attempted to specifically address the correlation between relative tumor content in αSMA^+ myofibroblasts and PDAC patient outcomes, potential therapeutic intervention prior to tumor resection makes interpretations unclear (Erkan et al., 2008; Mani et al., 2008).

Myofibroblast depletion leads to extensive remodeling of the tumor ECM, with a significant decrease in tumor tissue stiffness and total collagen content. Myofibroblasts contribute to the production of type I collagen, albeit likely not all of it. Contrary to previous assumptions, myofibroblasts do not contribute to the total production of LOX, an enzyme responsible for crosslinking of type I collagen. In this regard, we did not observe a difference in crosslinking, despite significant depletion and reorganization of tumor-associated collagen. Therefore, cancer cells or other stromal cells may compensate LOX expression. Similar to LOX, myofibroblast depletion did not affect HA content of the tumors, suggesting a nonmyofibroblast source for this matrix molecule. Targeting HA using PEGPH20, a modified enzyme that degrades HA, yielded promising results when combined with GEM (Jacobetz et al., 2013; Provenzano et al., 2012). In our study, ECM remodeling and the significant reduction in collagen content via myofibroblast depletion did not improve the treatment efficacy of GEM. Therefore, PDAC-associated myofibroblasts and type I collagen do not appear to serve as physical barriers to the exposure of cancer cells to GEM. In this regard, the potential role of HA, independent of type I collagen, in determining interstitial fluid pressure in PDAC tissue needs further mechanistic unraveling, and clinical trials with PEGPH20 will offer more insights in the future (Provenzano et al., 2012).

As noted above, significant depletion of myofibroblasts and type I collagen did not alter vessel permeability and perfusion. GEM efficacy was unaltered in myofibroblast and type I collagen-depleted tumors, suggesting that the increased efficacy observed in preclinical models treated with GEM and Smoothened inhibitor IPI-926 was likely due to mechanisms independent of myofibroblasts and type I collagen (Olive et al., 2009). It is likely that Smoothened inhibition was not myofibroblast specific and could also have affected other stromal cells, such as endothelial cells. In this regard, further analysis of the failed clinical trials could shed further light on this matter (Amakye et al., 2013). It is possible that if higher doses of IPI-926 combined with prolonged treatment period were used in the preclinical setting, potential adverse effects may have been encountered (Olive et al., 2009; Amakye et al., 2013). Nevertheless, our direct approach of targeting myofibroblasts and the associated fibrosis offers further insights into the complexity of using pharmacological targeting to derive specific answers related to target cells in tumors (Olive et al., 2009).

An interesting corollary that emerges from this study is the dominant contribution of cell division in the accumulation of myofibroblasts in PDAC. The origin of myofibroblasts in PDAC may be diverse (Phillips, 2012; Scarlett et al., 2011), yet using the αSMA-tk strategy to ablate proliferating myofibroblasts, we show 80% depletion of these cells, which account for the majority of myofibroblasts in PDAC tumors. These results offer an opportunity to speculate that drugs such as GEM and paclitaxel, which target proliferating cancer cells, may also target proliferating myofibroblasts. Such dual targeting may likely compromise the efficacy of GEM over time, because of progressive depletion of protective fibrosis along with proliferating cancer cells, resulting in the eventual emergence of resistant cancer cells with EMT program and stem cell-like phenotype.

Intratumoral hypoxia was dramatically increased in myofibroblast-depleted tumors. Decreased tumor vasculature, despite intact vessel structural integrity and permeability status, may have directly contributed to the increased tumor hypoxia when myofibroblasts are depleted, consequently promoting enhanced invasiveness and an undifferentiated phenotype of cancer cells (Cheresh and Stupack, 2008; Cooke et al., 2012; Pàez-Ribes et al., 2009). Impaired paracrine signaling between myofibroblasts and cancer cells and alteration of ECM microenvironment due to myofibroblast depletion might also have directly contributed to changes in cancer cells, lending to the acquisition of EMT program, stem cell-like phenotype, and an undifferentiated state. Many studies have indeed suggested that altered matrix microenvironment can influence the acquisition of epigenetic changes in epithelial cells (Bissell et al., 2005; Grassian et al., 2011; Guerra et al., 2011).

Figure 4. Myofibroblast-Depleted Tumors Display Increased Invasion Associated with Intratumoral Hypoxia

(A) Representative micrographs (scale bar represents 100 μm) of CD31 staining and corresponding quantification (n = 4). Dashed lines delineate the stromal compartment, where $CD31^+$ vessels are primarily found.

(B) Representative micrographs (scale bar represents 100 μm) and corresponding quantification (n = 4) of CD31 cells and intratumoral FITC-dextran leakage.

(C) Representative micrographs (scale bar represents 100 μm) of hypoxia indicator, Hypoxyprobe, and corresponding quantification (n = 4).

(D) Representative micrographs (scale bar represents 50 μm) of αSMA^+ cells in tumors with YFP^+ linage tagged cancer cells and corresponding quantification (n = 4). White arrowheads point to αSMA^+YFP^+ cells.

(E) Relative *Twist*, *Snail*, and *Slug* expression in tumors.

(F) Representative micrograph (scale bar represents 100 μm) of YFP^+ tumor spheres (insert shows higher magnification micrograph, scale bar represents 25 μm) and corresponding quantification (n = 15).

(G) Representative scatterplot and quantification of percentage $CD44^+CD133^+$ cancer cells (control: n = 2; depleted: n = 3). Q1: $CD44^+CD133^-$; Q2: $CD44^+CD133^+$; Q3: $CD44^-CD133^+$; Q4: $CD44^-CD133^-$.

(H) Tumorigenic ability of YFP^+ cells determined by limiting dilution assay. For each cell dose, six mice were injected with YFP^+ cancer cells from control or myofibroblast depleted tumors, and data are presented as the number of mice displaying tumors. Significance was assayed using χ^2 tests.

Data are represented as mean ± SEM. Unless otherwise noted, significance was determined using t tests (*$p < 0.05$, **$p < 0.01$, ****$p < 0.0001$). ns, not significant. See also Figure S4 and Table S3.

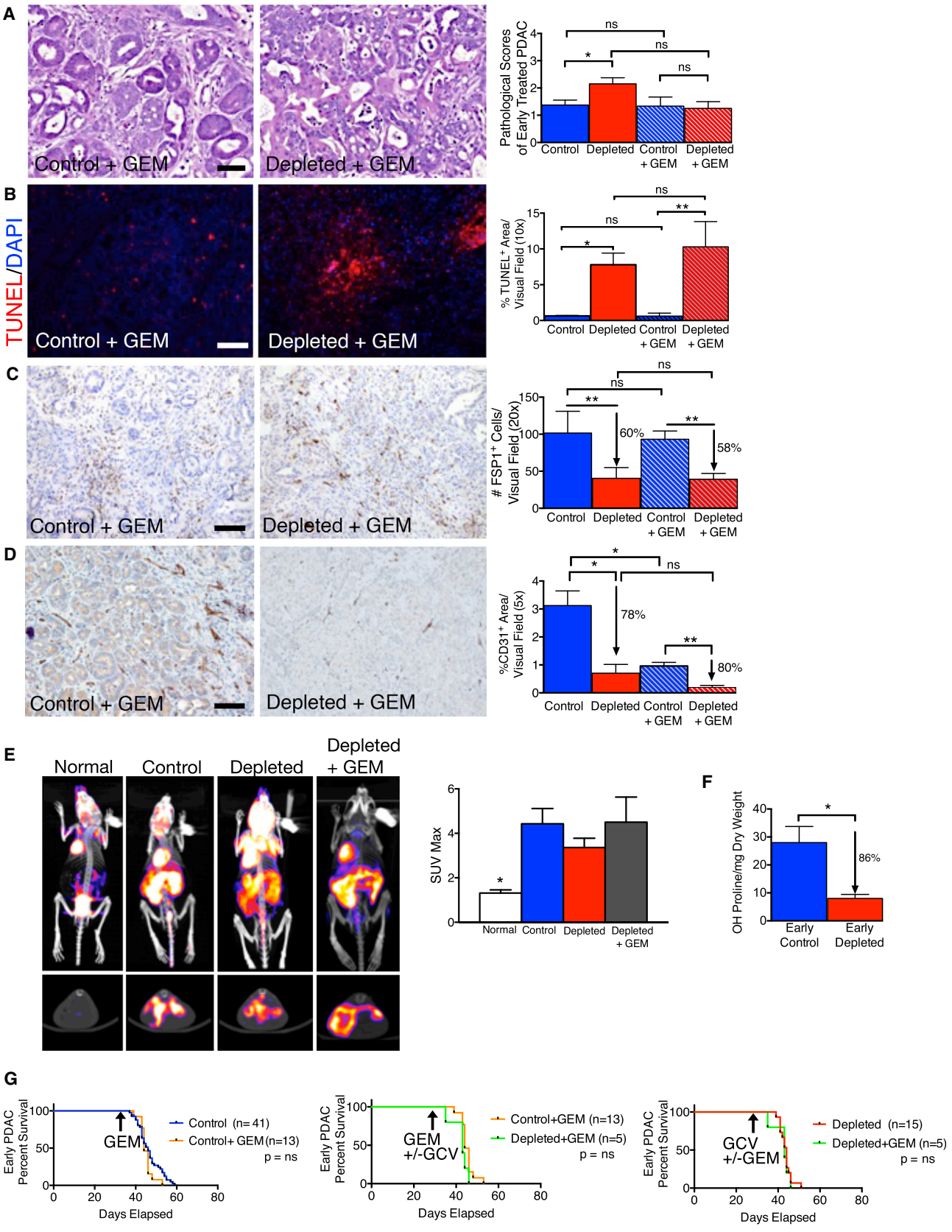

(legend on next page)

The most dramatic impact of myofibroblast depletion was on the composition of the immune infiltrate in the tumor microenvironment. The interplay between cancer-associated fibroblasts and immune cells has long been recognized as a major contributor of cancer development (Coussens and Werb, 2002; Erez et al., 2010; Kalluri and Zeisberg, 2006). Here, we demonstrate that the immune response (innate and adaptive) associated with PDAC tumors was significantly impaired when fibrosis was reduced starting at the PanIN stage or at the PDAC stage. Myofibroblast-depleted tumors are associated with a decreased Teff/Treg ratio and a significant elevation in *Ctla4* expression. Myofibroblast depletion coupled with inhibition of checkpoint blockade using anti-CTLA-4 antibodies significantly ameliorated tumor burden in mice with established PDAC and improved overall survival. Our data suggest that although myofibroblast depletion results in the suppression of immune surveillance, an opportunist immune profile dominated by suppressor T cells emerges in the tumor, offering a viable checkpoint blockade target using anti-CTLA-4 antibodies. Although this antibody shows marginal efficacy in control PDAC mice with normal levels of fibrosis, depletion of fibrosis unravels more robust efficacy, likely because of significant changes in the microenvironment. Small proof-of-concept trials with ipilimumab have revealed some anecdotal responses (Royal et al., 2010), and our study suggests that stratifying patients on the basis of their fibrosis scores might offer better responses. This is supported by the fact that ipilimumab showed dramatic efficacy in metastatic melanoma (Robert et al., 2011), a cancer with low levels of overall stroma.

In summary, our study, together with other ongoing efforts to elucidate pancreatic tumor immunity and immunotherapy (Bayne et al., 2012; Clark et al., 2007; Hiraoka et al., 2006; Roberts et al., 2013; Vonderheide et al., 2013), will likely offer insights into potential efficacy of combination therapies involving immunotherapy in patients with pancreas cancer.

EXPERIMENTAL PROCEDURES

Animal Studies

The disease progression and genotyping for the PKT mice was previously described (Ijichi et al., 2006). PKT mice were crossed to R26-*LSL*-EYFP (purchased from Jackson Laboratory), αSMA-tk (LeBleu et al., 2013), and αSMA-RFP (LeBleu et al., 2013) mice. Mice received daily intraperitoneal (i.p.) injections with 50 mg/kg body weight of GCV at 4 to 4.5 weeks of age (30.3 ± 1.7 days) for 14 days or less (early depletion) or at 6 weeks of age (40.7 ± 1.7 days) for 10 days or less (late depletion). One hour prior to sacrifice, mice were injected i.p. with 60 mg/kg body weight pimonidazole (Hypoxyprobe). KPC mice were previously described (Hingorani et al., 2005) and crossed to αSMA-tk mice. KPC mice were treated with GCV starting at 7 weeks of age (49 ± 2.5 days). GEM (50 μg/kg body weight; LC Laboratories) was given i.p. at day 1 and day 7, either alone or in combination with GCV. An initial 200 μg anti-CTLA-4 (BioXCell, clone 9H10, BE0131) antibody or 200 μg hamster immunoglobulin G (IgG) (BioXCell, BE0091) in 200 μl PBS was administered i.p., followed by two injections of 100 μg anti-CTLA-4 or 100 μg hamster IgG in 100 μl PBS every other day. All mice were housed under standard housing conditions at the Beth Israel Deaconess Medical Center (BIDMC) and MD Anderson Cancer Center (MDACC) animal facilities, and all animal procedures were reviewed and approved by the BIDMC and the MDACC institutional animal care and use committees. Acquisition and analysis of ^{18}F-FDG PET/CT in mice is detailed in Supplemental Experimental Procedures.

Histology and Histopathology

Formalin-fixed tumors were submitted to the BIDMC and MDACC histology core facilities, and paraffin-embedded sections were cut for hematoxylin and eosin (H&E) staining and MTS. For histopathological scoring, H&E-stained slides were scored for the penetrance of each histological hallmark on a scale of 0 to 3. The predominant tumor phenotype gave the pathological score for the whole tumor (1 = well differentiated, 2 = moderately differentiated, 3 = poorly differentiated). Necrosis was also scored on a scale of 0 to 3. Lung emboli were counted in one H&E lung section per mouse evaluated. Picrosirius red staining for collagen was achieved using 0.1% picrosirius red (Direct Red 80; Sigma) and counterstained with Weigert's hematoxylin. Mucin staining was achieved using mucicarmine and metalin yellow and counter-stained with Weigert's hematoxylin.

IHC

Harvested tumors were formalin fixed prior to paraffin embedding. Sections 4 to 5 μm thick were deparaffinized, rehydrated, and boiled for 1 hr in 10 mM citrate buffer at pH 6.0. Staining for αSMA was processed using the M.O.M. Kit (Vector Laboratories) according to the manufacturer's recommendations. For all other stains, the tissue sections were blocked with 1% BSA in Tris-buffered saline for 30 min prior to incubation with the primary antibody. Sections were then incubated with biotin-conjugated anti-rabbit/rat/goat IgG and ABC reagent (Vector Laboratories) for 30 to 45 min at room temperature. DAB was used as a detection system (Vector Laboratories) according to the manufacturer's instructions. The following primary antibodies were used: mouse anti-αSMA (Sigma) 1:200, rabbit anti-FSP1 (a gift from Dr. Eric Nielson, Northwestern University Feinberg School of Medicine) 1:50, biotinylated anti-HABP (Amsbio) 1:200, rabbit anti-CD31 (Abcam) 1:50, and rabbit antivimentin (Cell Signaling) 1:100. For all stainings, DAB positivity was analyzed in five to eight visual fields at an original magnification of 10×, 20×, or 40×. Control and treated mice within an experimental set (at least three mice per group) were analyzed. All stainings were quantified using NIH ImageJ analysis software with the same threshold for each stain; results were expressed as percentage staining per visual field.

Immunofluorescence

Harvested tumors were embedded in O.C.T. medium (TissueTek). Frozen sections 4 to 5 μm thick were fixed in ice-cold acetone for 20 min, blocked

Figure 5. GEM Treatment Does Not Improve Survival of Mice with Myofibroblast-Depleted Tumors

(A) Representative micrographs of H&E stained pancreatic samples (scale bar represents 100 μm) and pathological scores of indicated experimental groups. Control, n = 16; depleted, n = 17; GEM, n = 8; and GEM depleted, n = 8.

(B) Representative micrographs (scale bar represents 200 μm) of the apoptosis marker TUNEL and corresponding quantification (n = 3 in each group).

(C) Representative micrographs (scale bar represents 100 μm) of FSP1 IHC and corresponding quantification (n = 4 in each group).

(D) Representative micrographs (scale bar represents 100 μm) of CD31 IHC and corresponding quantification (n = 3 in each group).

(E) Representative ^{18}F-FDG PET/CT (top, frontal section; bottom, sagittal section) and associated maximum standard update value (SUVmax) (n = 3 in each group).

(F) Hydroxyproline release reflecting collagen content in control and myofibroblast-depleted tumors (n = 4 in each group). Significance was determined using t tests.

(G) Survival analyses of indicated experimental groups.

Data are represented as mean ± SEM. Unless otherwise noted, significance was determined using one-way ANOVA with Tukey post hoc analysis (*$p < 0.05$, **$p < 0.01$). ns, not significant.

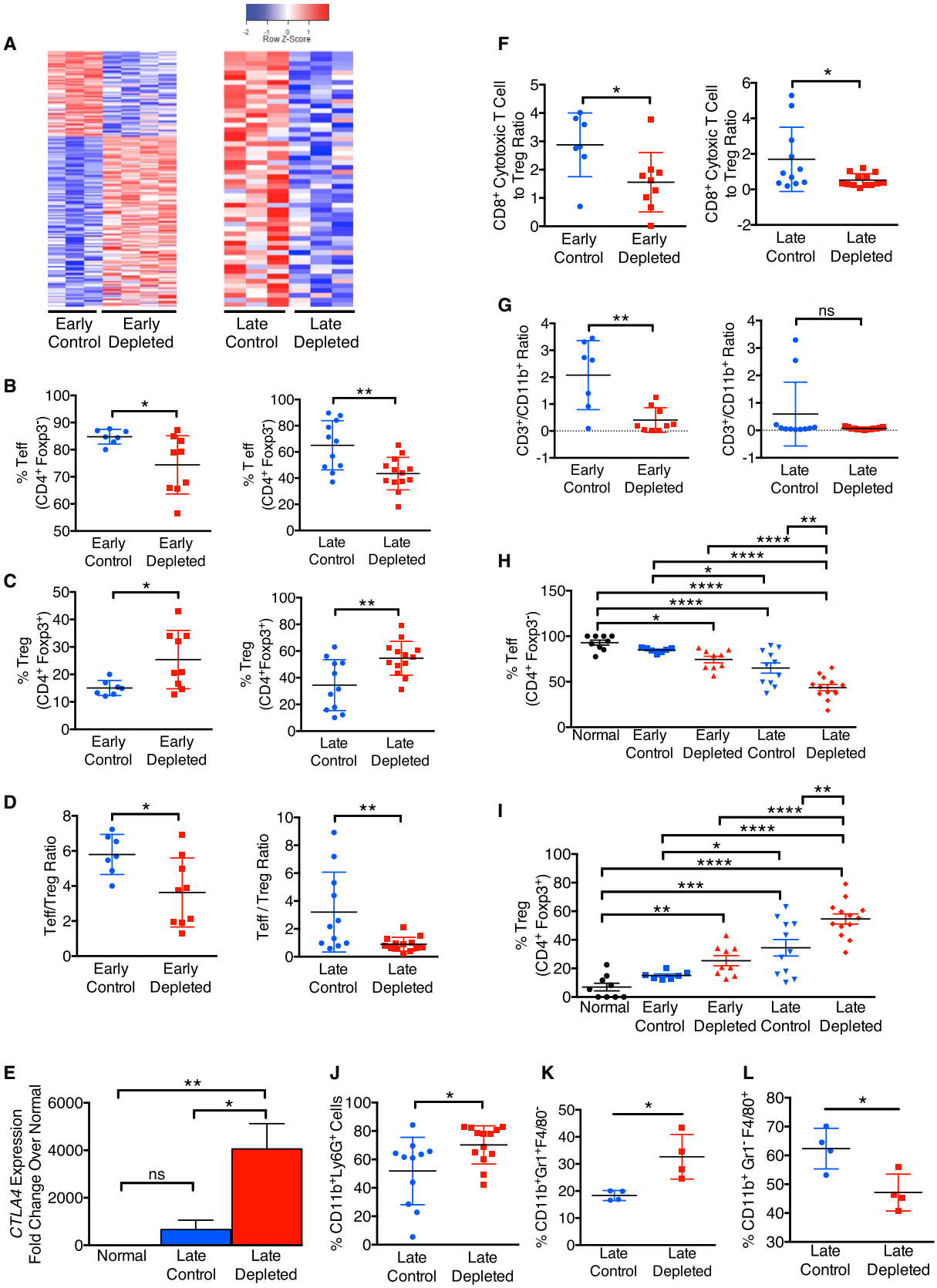

(legend on next page)

with 1% BSA in PBS, and immunostained using standard protocols. Primary antibodies used were goat anti-collagen 1 (Southern Biotech) 1:200, mouse anti-αSMA-FITC/mouse anti-αSMA-Cy3 (Sigma) 1:200, rat antimouse Ki-67 (abcam) 1:200, rabbit anti-FAP (Abcam) 1:200, rat anti-foxp3 (eBioscience) 1:150, rabbit anti-NG2 (Millipore) 1:200, rat anti-CD31 (BD PharMingen) 1:200, mouse 4.3.11.3 (Hypoxyprobe) 1:50, and rabbit anti-LOX (Imgenex) 1:200. Stainings for pimonidazole adduct (Hypoxyprobe) was processed using the M.O.M. Kit according to the manufacturer's recommendations. Apoptosis was assessed using In Situ Cell Death Detection Kit, TMR red (Roche). DAPI was used to stain cell nuclei.

Flow Cytometry

Weighed tumors were minced and allowed to digest in a 2 ml mixture of collagenase (400 U type II collagenase; Worthington) and 0.2 mg/ml DNase I in RPMI media at 37°C for 1 hr. The mixture was gently vortexed every 10 to 20 min. The tissue lysate was filtered through a 40 μm mesh prior to immunostaining. The resulting single-cell suspension was stained with fixable viability dye eFluor 780, anti-CD45.2 Pacific Blue, anti-CD3 PE-Cy7, anti-CD3 Alexa Fluor 700, anti-Foxp3 Alexa Fluor 700, anti-CD11c eFluor 615, and anti-NK1.1 PE (all from eBioscience); anti-Granzyme B APC and anti-CD4 Qdot 605 (Life Technologies); anti-CD8 Brilliant Violet 650, anti-CD11b Brilliant Violet 570, anti-CD19 Brilliant Violet 650, and anti-F4/80 FITC (all from BioLegend); and anti-Ly6C APC, anti-Ly6G PE-Cy7, and anti-Ki-67 PE (BD Biosciences). The percentage positive cells were analyzed by FlowJo and gated on CD45 positivity. To analyze the number of $CD133^+CD44^+$ cells, the single-cell suspension was incubated in the dark, on ice, with Aqua LIVE/DEAD Fixable Dead Cell Stain (Molecular Probes) 1:1,000 for 30 min, followed by staining with anti-CD44 APC 1:400 (eBioscience) and anti-CD133 PE 1:200 (eBioscience). Unstained, LIVE/DEAD only, and single stain served as control. Doublets were gated out using forward-scatter width/height and sideward-scatter width/height event characteristics.

Tumor Spheres and Limiting Dilution Tumor Formation Assay

Tumors were digested as described above, and cell suspension was filtered through a 100 μm mesh. Two million cells were plated in a low-adherence dish with 1% fetal bovine serum, Dulbecco's modified Eagle's medium, and penicillin/streptomycin/amphotericin. Three to 4 weeks later, the formed spheres were counted at 200× magnification. For the limiting dilution assay, flow cytometry purified YFP^+ cancer cells (from PKT mice crossed to R26-stop-EYFP reporter mice) were pelleted and resuspended in PBS prior to subcutaneous injection in nude mice. Six nude mice received injections of YFP^+ cells (100, 1,000 or 10,000 cells) from tumors of PKT mice without myofibroblast depletion (control; two donor mice were used) or with myofibroblast depletion (depleted; two donor mice were used).

Gene Expression Profiling

Total RNA was isolated from tumors of PKT control mice (n = 3 at early stage, n = 3 at late stage) and myofibroblast-depleted mice (n = 4 at early stage, n = 3 at late stage, n = 2 at late stage and treated with anti-CTLA4) using RNeasy Plus Mini Kit (Qiagen) and submitted to the Microarray Core Facility at MD Anderson Cancer Center. Gene expression analysis was performed using Mouse Ref6 Gene Expression BeadChip (Illumina), and the Limma package from R Bioconductor (Carey et al., 2005) was used to analyze differentially expressed genes of myofibroblast-depleted mice versus control mice ($p \leq 0.05$, fold change ≥ 1.5). Gene ontology and pathway analyses of differentially expressed genes are performed using the Web-accessible program Database for Annotation, Visualization and Integrated Discovery (Huang et al., 2009). Pathways that enrich differentially expressed genes are selected ($p < 0.05$). For RNA sequencing analyses, sequencing of the whole transcriptome was performed using the SOLiD system. Lifescope Genomic Analysis Software version 2.5.1 was used to map the raw data to the mouse genome (build mm10) and to quantify the counts per gene. The count data were used to perform differential expression analysis using the R package, DEseq. Quantitative real-time PCR analyses are detailed in Supplemental Experimental Procedures.

Vascular Leakage

Vascular leakage was assayed and quantified as previously described (Cooke et al., 2012). Quantification was performed using a grading system ranging from 0 to 5, representing 0% to 100% extravascular FITC-dextran. Results were plotted as scores.

Clinical Studies

Resected tumors were obtained from 53 patients (Table S1) with invasive pancreatic adenocarcinoma who underwent surgical resection at Johns Hopkins Hospital after approval by the Johns Hopkins Hospital institutional review board (IRB). The cases were obtained under an IRB-exempt protocol. Clinical information was obtained from the electronic medical records. Tissue sections from paraffin-embedded specimens were stained for αSMA (Sigma) as described above, and staining intensity was scored blinded. Each tissue section was surveyed entirely for αSMA stain intensity in interstitial fibroblasts. $αSMA^+$ vessels of all sizes were easily distinguishable from interstitial fibroblasts. Overall, few $αSMA^+$ vessels were detected in the tumors, and these were not included in the score. A scale of 0 to 3 was used (0 = no detected staining, 1 = weak staining, 2 = moderate staining, 3 = strong staining). Patients were then divided into two groups: a "low αSMA" group, as defined by scores of 0 and 1, and a "high αSMA" group, as defined by scores of 2 and 3. Kaplan-Meier plots were drawn for each group and statistical differences evaluated using the log rank Mantel-Cox test.

Statistics

Statistical analyses of pathological scores, flow cytometry, and immunohistochemical quantifications were performed by using Student's t test, one-way ANOVA, or Fisher's exact test with GraphPad Prism (GraphPad Software). Limiting dilution assay was evaluated using SPSS (SPSS) with chi-square tests. For survival analyses, Kaplan-Meier plots were drawn and statistical differences evaluated using the log rank Mantel-Cox test. A p value < 0.05 was considered statistically significant.

ACCESSION NUMBERS

The microarray data are deposited at Gene Expression Omnibus under accession numbers GSE52812 (gene expression changes comparing pancreas tumors from PKT mice with pancreas tumors from PKT; αSMA-tk mice) and GSE55871 (gene expression changes comparing myofibroblasts from pancreas tumors of PKT mice with myofibroblasts from pancreas tumors of PKT; αSMA-tk mice).

SUPPLEMENTAL INFORMATION

Supplemental Information includes Supplemental Experimental Procedures, six figures, and three tables and can be found with this article online at http://dx.doi.org/10.1016/j.ccr.2014.04.005.

Figure 6. Myofibroblast Depletion Results in Increased Frequency of $FoxP3^+$ Treg Cells in PDAC

(A) Heatmap of differentially regulated genes pertaining to tumor immunity in early- and late-treated tumors.
(B–D) Percentage Teff (B), percentage Treg (C), and Teff/Treg ratio (D) in early- and late-treated tumors.
(E) Relative *Ctla4* expression in late-treated tumors (n = 6).
(F and G) $CD8^+$ cytotoxic T cell/Treg ratio (F) and CD3/CD11b ratio (G) in early- and late-treated tumors.
(H and I) Percentages Teff (H) and Treg (I) in normal pancreas and in early- and late-treated tumors.
(J–L) Percentages $CD11b^+Ly6G^+$ (J), $CD11b^+Gr1^+F4/80^-$ (K), and $CD11b^+Gr1^-F4/80^+$ (L) cells in late-treated tumors.
Data are represented as mean ± SEM. Significance was determined using t tests, except for multiple-group comparisons, for which significance was determined using one-way ANOVA with Tukey post hoc analysis (*$p < 0.05$, **$p < 0.01$, **$p < 0.001$, ****$p < 0.0001$). ns, not significant. See also Figure S5.

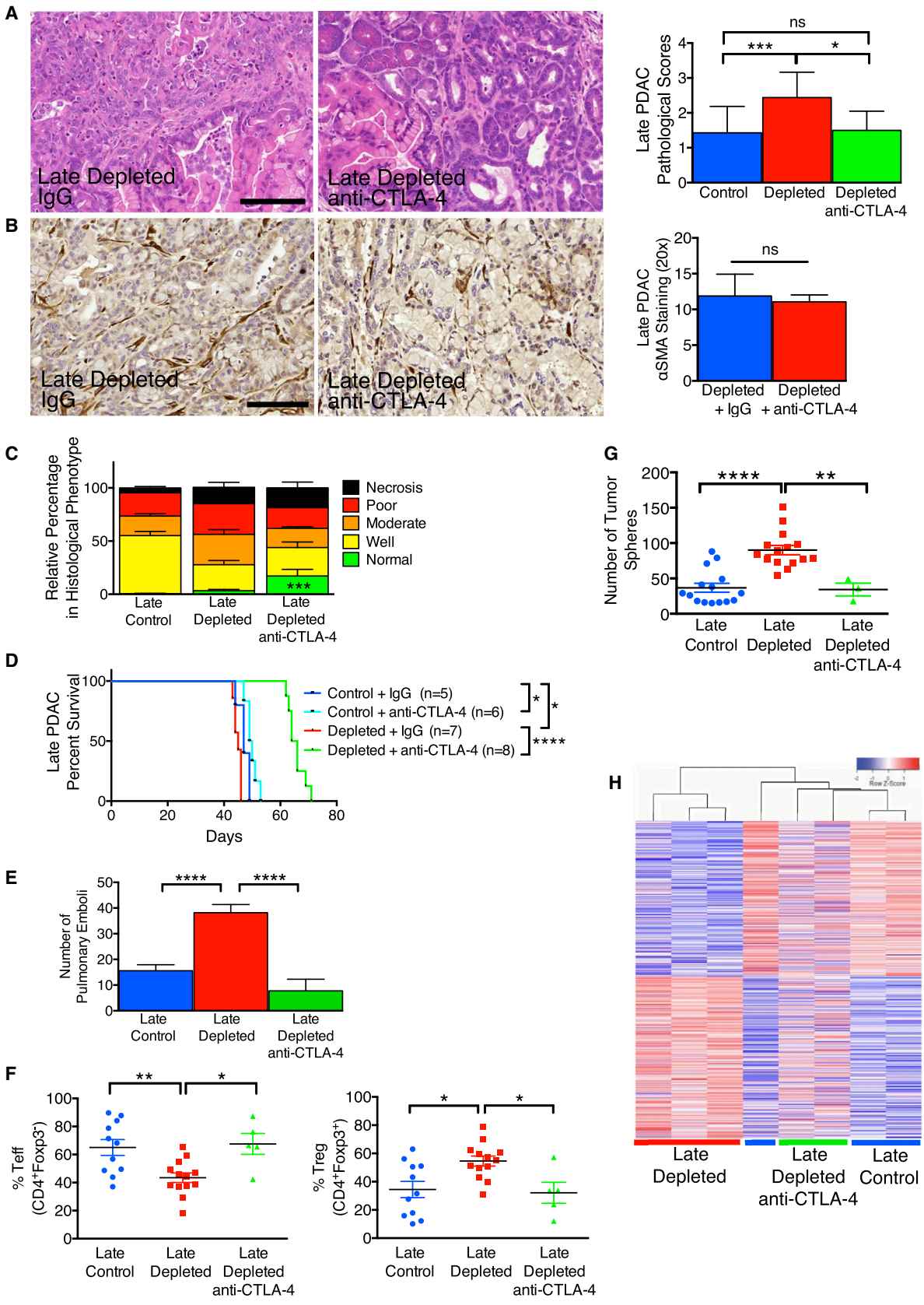

(legend on next page)

ACKNOWLEDGMENTS

We wish to thank Travis Hardcastle, Lauren Bizarro, Judith Kaye, Laura Gibson, and Sara Lovisa for genotyping and animal husbandry support; Donna Reynolds for IHC stainings; and Travis Hardcastle, Dr. Ganiraju C. Manyam, Dr. Jing Wang, and the Bioinformatics and Computational Biology Department at MDACC for bioinformatic support. This study was supported primarily by NIH grant UO1 CA151925. B.C.O. received funding from the OncoSuisse MD/PhD Scholarship (323630-128865/1) and the Swiss National Science Foundation Fellowship (PBBEP3_144809). C.K. is funded by a Research Fellowship of Deutsche Forschungsgemeinschaft. A.M. is supported by NIH grant CA113669. R.K. is supported by the Cancer Prevention and Research Institute of Texas and the Metastasis Research Center at MD Anderson Cancer Center, NIH grants DK55001, DK81976, CA125550, CA155370, and CA163191. J.P.A. is an inventor of intellectual property owned by the University of California, Berkeley, and licensed to Bristol Myers-Squibb.

Received: January 6, 2014
Revised: February 8, 2014
Accepted: April 10, 2014
Published: May 22, 2014

REFERENCES

Aguirre, A.J., Bardeesy, N., Sinha, M., Lopez, L., Tuveson, D.A., Horner, J., Redston, M.S., and DePinho, R.A. (2003). Activated Kras and Ink4a/Arf deficiency cooperate to produce metastatic pancreatic ductal adenocarcinoma. Genes Dev. *17*, 3112–3126.

Amakye, D., Jagani, Z., and Dorsch, M. (2013). Unraveling the therapeutic potential of the Hedgehog pathway in cancer. Nat. Med. *19*, 1410–1422.

Angeli, F., Koumakis, G., Chen, M.C., Kumar, S., and Delinassios, J.G. (2009). Role of stromal fibroblasts in cancer: promoting or impeding? Tumour Biol. *30*, 109–120.

Armstrong, T., Packham, G., Murphy, L.B., Bateman, A.C., Conti, J.A., Fine, D.R., Johnson, C.D., Benyon, R.C., and Iredale, J.P. (2004). Type I collagen promotes the malignant phenotype of pancreatic ductal adenocarcinoma. Clin. Cancer Res. *10*, 7427–7437.

Bardeesy, N., Aguirre, A.J., Chu, G.C., Cheng, K.H., Lopez, L.V., Hezel, A.F., Feng, B., Brennan, C., Weissleder, R., Mahmood, U., et al. (2006a). Both p16(Ink4a) and the p19(Arf)-p53 pathway constrain progression of pancreatic adenocarcinoma in the mouse. Proc. Natl. Acad. Sci. USA *103*, 5947–5952.

Bardeesy, N., Cheng, K.H., Berger, J.H., Chu, G.C., Pahler, J., Olson, P., Hezel, A.F., Horner, J., Lauwers, G.Y., Hanahan, D., and DePinho, R.A. (2006b). Smad4 is dispensable for normal pancreas development yet critical in progression and tumor biology of pancreas cancer. Genes Dev. *20*, 3130–3146.

Bayne, L.J., Beatty, G.L., Jhala, N., Clark, C.E., Rhim, A.D., Stanger, B.Z., and Vonderheide, R.H. (2012). Tumor-derived granulocyte-macrophage colony-stimulating factor regulates myeloid inflammation and T cell immunity in pancreatic cancer. Cancer Cell *21*, 822–835.

Bissell, M.J., and Radisky, D. (2001). Putting tumours in context. Nat. Rev. Cancer *1*, 46–54.

Bissell, M.J., Kenny, P.A., and Radisky, D.C. (2005). Microenvironmental regulators of tissue structure and function also regulate tumor induction and progression: the role of extracellular matrix and its degrading enzymes. Cold Spring Harb. Symp. Quant. Biol. *70*, 343–356.

Carey, V.J., Dudoit, R., Irizarry, R., Huber, W., and Gentleman, R. (2005). Bioinformatics and Computational Biology Solutions Using R and Bioconductor. (Bioconductor), http://www.bioconductor.org/help/publications/books/bioinformatics-and-computational-biology-solutions/

Cheresh, D.A., and Stupack, D.G. (2008). Regulation of angiogenesis: apoptotic cues from the ECM. Oncogene *27*, 6285–6298.

Clark, C.E., Hingorani, S.R., Mick, R., Combs, C., Tuveson, D.A., and Vonderheide, R.H. (2007). Dynamics of the immune reaction to pancreatic cancer from inception to invasion. Cancer Res. *67*, 9518–9527.

Cooke, V.G., LeBleu, V.S., Keskin, D., Khan, Z., O'Connell, J.T., Teng, Y., Duncan, M.B., Xie, L., Maeda, G., Vong, S., et al. (2012). Pericyte depletion results in hypoxia-associated epithelial-to-mesenchymal transition and metastasis mediated by met signaling pathway. Cancer Cell *21*, 66–81.

Coussens, L.M., and Werb, Z. (2002). Inflammation and cancer. Nature *420*, 860–867.

Dvorak, H.F. (1986). Tumors: wounds that do not heal. Similarities between tumor stroma generation and wound healing. N. Engl. J. Med. *315*, 1650–1659.

Erez, N., Truitt, M., Olson, P., Arron, S.T., and Hanahan, D. (2010). Cancer-associated fibroblasts are activated in incipient neoplasia to orchestrate tumor-promoting inflammation in an NF-kappaB-dependent manner. Cancer Cell *17*, 135–147.

Erkan, M., Michalski, C.W., Rieder, S., Reiser-Erkan, C., Abiatari, I., Kolb, A., Giese, N.A., Esposito, I., Friess, H., and Kleeff, J. (2008). The activated stroma index is a novel and independent prognostic marker in pancreatic ductal adenocarcinoma. Clin. Gastroenterol. Hepatol. *6*, 1155–1161.

Feig, C., Gopinathan, A., Neesse, A., Chan, D.S., Cook, N., and Tuveson, D.A. (2012). The pancreas cancer microenvironment. Clin. Cancer Res. *18*, 4266–4276.

Gidekel Friedlander, S.Y., Chu, G.C., Snyder, E.L., Girnius, N., Dibelius, G., Crowley, D., Vasile, E., DePinho, R.A., and Jacks, T. (2009). Context-dependent transformation of adult pancreatic cells by oncogenic K-Ras. Cancer Cell *16*, 379–389.

Grassian, A.R., Coloff, J.L., and Brugge, J.S. (2011). Extracellular matrix regulation of metabolism and implications for tumorigenesis. Cold Spring Harb. Symp. Quant. Biol. *76*, 313–324.

Guerra, C., Collado, M., Navas, C., Schuhmacher, A.J., Hernández-Porras, I., Cañamero, M., Rodriguez-Justo, M., Serrano, M., and Barbacid, M. (2011). Pancreatitis-induced inflammation contributes to pancreatic cancer by inhibiting oncogene-induced senescence. Cancer Cell *19*, 728–739.

Hermann, P.C., Huber, S.L., Herrler, T., Aicher, A., Ellwart, J.W., Guba, M., Bruns, C.J., and Heeschen, C. (2007). Distinct populations of cancer stem cells

Figure 7. Anti-CTLA-4 Attenuates PDAC and Improves Survival in Mice with Myofibroblast-Depleted Tumors

(A) Representative micrographs of H&E stained tumors (scale bar represents 100 μm) and pathological scores of tumors in indicated experimental groups. Control, n = 14; depleted, n = 16; depleted plus anti-CTLA-4, n = 6. Significance was determined using one-way ANOVA with Tukey post hoc analysis.

(B) Representative micrographs of αSMA stained pancreatic samples (scale bar represents 100 μm) and corresponding quantification. Depleted, n = 5; depleted plus anti-CTLA-4, n = 7.

(C) Relative percentage of tissue encompassed by each histology hallmark. Control, n = 15; depleted, n = 16; depleted plus anti-CTLA-4, n = 6. Significance was determined using one-way ANOVA with Tukey post hoc analysis.

(D) Survival analysis of the indicated experimental groups.

(E) Number of pulmonary emboli. Control, n = 14; depleted, n = 28; depleted plus anti-CTLA-4, n = 8.

(F) Percentages Teff (left) and Treg (right) cells in tumors of indicated experimental groups.

(G) Number of spheres formed from tumors of indicated experimental groups.

(H) Heatmap of differentially expressed genes in the indicated groups.

Data are represented as mean ± SEM. Unless otherwise noted, significance was determined using t tests (*$p < 0.05$, **$p < 0.01$, **$p < 0.001$, ****$p < 0.0001$). ns, not significant. See also Figure S6.

determine tumor growth and metastatic activity in human pancreatic cancer. Cell Stem Cell *1*, 313–323.

Hidalgo, M. (2010). Pancreatic cancer. N. Engl. J. Med. *362*, 1605–1617.

Hingorani, S.R., Petricoin, E.F., Maitra, A., Rajapakse, V., King, C., Jacobetz, M.A., Ross, S., Conrads, T.P., Veenstra, T.D., Hitt, B.A., et al. (2003). Preinvasive and invasive ductal pancreatic cancer and its early detection in the mouse. Cancer Cell *4*, 437–450.

Hingorani, S.R., Wang, L., Multani, A.S., Combs, C., Deramaudt, T.B., Hruban, R.H., Rustgi, A.K., Chang, S., and Tuveson, D.A. (2005). Trp53R172H and KrasG12D cooperate to promote chromosomal instability and widely metastatic pancreatic ductal adenocarcinoma in mice. Cancer Cell *7*, 469–483.

Hiraoka, N., Onozato, K., Kosuge, T., and Hirohashi, S. (2006). Prevalence of FOXP3+ regulatory T cells increases during the progression of pancreatic ductal adenocarcinoma and its premalignant lesions. Clin. Cancer Res. *12*, 5423–5434.

Hruban, R.H., Pitman, M.B., and Klimstra, D.S. (2007). Tumors of the Pancreas. (Washington: American Registry of Pathology).

Huang, W., Sherman, B.T., and Lempicki, R.A. (2009). Systematic and integrative analysis of large gene lists using DAVID bioinformatics resources. Nat. Protoc. *4*, 44–57.

Ijichi, H., Chytil, A., Gorska, A.E., Aakre, M.E., Fujitani, Y., Fujitani, S., Wright, C.V., and Moses, H.L. (2006). Aggressive pancreatic ductal adenocarcinoma in mice caused by pancreas-specific blockade of transforming growth factor-beta signaling in cooperation with active Kras expression. Genes Dev. *20*, 3147–3160.

Jacobetz, M.A., Chan, D.S., Neesse, A., Bapiro, T.E., Cook, N., Frese, K.K., Feig, C., Nakagawa, T., Caldwell, M.E., Zecchini, H.I., et al. (2013). Hyaluronan impairs vascular function and drug delivery in a mouse model of pancreatic cancer. Gut *62*, 112–120.

Kalluri, R., and Zeisberg, M. (2006). Fibroblasts in cancer. Nat. Rev. Cancer *6*, 392–401.

Kalluri, R., and Weinberg, R.A. (2009). The basics of epithelial-mesenchymal transition. J. Clin. Invest. *119*, 1420–1428.

Karnoub, A.E., Dash, A.B., Vo, A.P., Sullivan, A., Brooks, M.W., Bell, G.W., Richardson, A.L., Polyak, K., Tubo, R., and Weinberg, R.A. (2007). Mesenchymal stem cells within tumour stroma promote breast cancer metastasis. Nature *449*, 557–563.

Korc, M. (2007). Pancreatic cancer-associated stroma production. Am. J. Surg. *194*, S84–S86.

LeBleu, V.S., Taduri, G., O'Connell, J., Teng, Y., Cooke, V.G., Woda, C., Sugimoto, H., and Kalluri, R. (2013). Origin and function of myofibroblasts in kidney fibrosis. Nat. Med. *19*, 1047–1053.

Lu, P., Weaver, V.M., and Werb, Z. (2012). The extracellular matrix: a dynamic niche in cancer progression. J. Cell Biol. *196*, 395–406.

Mani, S.A., Guo, W., Liao, M.J., Eaton, E.N., Ayyanan, A., Zhou, A.Y., Brooks, M., Reinhard, F., Zhang, C.C., Shipitsin, M., et al. (2008). The epithelial-mesenchymal transition generates cells with properties of stem cells. Cell *133*, 704–715.

Merika, E.E., Syrigos, K.N., and Saif, M.W. (2012). Desmoplasia in pancreatic cancer. Can we fight it? Gastroenterol. Res. Pract. *2012*, 781765.

Olive, K.P., Jacobetz, M.A., Davidson, C.J., Gopinathan, A., McIntyre, D., Honess, D., Madhu, B., Goldgraben, M.A., Caldwell, M.E., Allard, D., et al. (2009). Inhibition of Hedgehog signaling enhances delivery of chemotherapy in a mouse model of pancreatic cancer. Science *324*, 1457–1461.

Omary, M.B., Lugea, A., Lowe, A.W., and Pandol, S.J. (2007). The pancreatic stellate cell: a star on the rise in pancreatic diseases. J. Clin. Invest. *117*, 50–59.

Pàez-Ribes, M., Allen, E., Hudock, J., Takeda, T., Okuyama, H., Viñals, F., Inoue, M., Bergers, G., Hanahan, D., and Casanovas, O. (2009). Antiangiogenic therapy elicits malignant progression of tumors to increased local invasion and distant metastasis. Cancer Cell *15*, 220–231.

Phillips, P. (2012). Pancreatic stellate cells and fibrosis. In Pancreatic Cancer and Tumor Microenvironment, P.J. Grippo and H.G. Munshi, eds. (Trivandrum: Transworld Research Network), chap. 3.

Provenzano, P.P., Cuevas, C., Chang, A.E., Goel, V.K., Von Hoff, D.D., and Hingorani, S.R. (2012). Enzymatic targeting of the stroma ablates physical barriers to treatment of pancreatic ductal adenocarcinoma. Cancer Cell *21*, 418–429.

Rasheed, Z.A., Matsui, W., and Maitra, A. (2012). Pathology of pancreatic stroma in PDAC. In Pancreatic Cancer and Tumor Microenvironment, P.J. Grippo and H.G. Munshi, eds. (Trivandrum: Transworld Research Network), chap. 1.

Robert, C., Thomas, L., Bondarenko, I., O'Day, S., Webster, J.W., Garbe, C., Lebbe, C., Baurain, J.F., Testori, A., Grob, J.J., et al. (2011). Ipilimumab plus dacarbazine for previously untreated metastatic melanoma. N. Engl. J. Med. *364*, 2517–2526.

Roberts, E.W., Deonarine, A., Jones, J.O., Denton, A.E., Feig, C., Lyons, S.K., Espeli, M., Kraman, M., McKenna, B., Wells, R.J., et al. (2013). Depletion of stromal cells expressing fibroblast activation protein-α from skeletal muscle and bone marrow results in cachexia and anemia. J. Exp. Med. *210*, 1137–1151.

Royal, R.E., Levy, C., Turner, K., Mathur, A., Hughes, M., Kammula, U.S., Sherry, R.M., Topalian, S.L., Yang, J.C., Lowy, I., and Rosenberg, S.A. (2010). Phase 2 trial of single agent ipilimumab (anti-CTLA-4) for locally advanced or metastatic pancreatic adenocarcinoma. J. Immunother. *33*, 828–833.

Scarlett, C.J., Colvin, E.K., Pinese, M., Chang, D.K., Morey, A.L., Musgrove, E.A., Pajic, M., Apte, M., Henshall, S.M., Sutherland, R.L., et al. (2011). Recruitment and activation of pancreatic stellate cells from the bone marrow in pancreatic cancer: a model of tumor-host interaction. PLoS ONE *6*, e26088.

Scheel, C., and Weinberg, R.A. (2012). Cancer stem cells and epithelial-mesenchymal transition: concepts and molecular links. Semin. Cancer Biol. *22*, 396–403.

Simeone, D.M. (2008). Pancreatic cancer stem cells: implications for the treatment of pancreatic cancer. Clin. Cancer Rese. *14*, 5646–5648.

Tsai, J.H., Donaher, J.L., Murphy, D.A., Chau, S., and Yang, J. (2012). Spatiotemporal regulation of epithelial-mesenchymal transition is essential for squamous cell carcinoma metastasis. Cancer Cell *22*, 725–736.

Vega, S., Morales, A.V., Ocaña, O.H., Valdés, F., Fabregat, I., and Nieto, M.A. (2004). Snail blocks the cell cycle and confers resistance to cell death. Genes Dev. *18*, 1131–1143.

Vonderheide, R.H., Bajor, D.L., Winograd, R., Evans, R.A., Bayne, L.J., and Beatty, G.L. (2013). CD40 immunotherapy for pancreatic cancer. Cancer Immunol. Immunother. *62*, 949–954.

Vong, S., and Kalluri, R. (2011). The role of stromal myofibroblast and extracellular matrix in tumor angiogenesis. Genes Cancer *2*, 1139–1145.

Wang, W.Q., Liu, L., Xu, H.X., Luo, G.P., Chen, T., Wu, C.T., Xu, Y.F., Xu, J., Liu, C., Zhang, B., et al. (2013). Intratumoral α-SMA enhances the prognostic potency of CD34 associated with maintenance of microvessel integrity in hepatocellular carcinoma and pancreatic cancer. PLoS ONE *8*, e71189.

Whatcott, C.J., Posner, R.G., Von Hoff, D.D., and Han, H. (2012). Desmoplasia and chemoresistance in pancreatic cancer. In Pancreatic Cancer and Tumor Microenvironment, P.J. Grippo and H.G. Munshi, eds. (Trivandrum: Transworld Research Network), chap. 8.